BeBeC-2026-S08

SEPARATING JET NOISE FROM OTHER ENGINE NOISE SOURCES IN STATIC TESTS

Pieter Sijtsma[1,2]
[1]PSA3, De Punt, 9493 TE, The Netherlands
[2]Faculty of Aerospace Engineering, TU Delft, The Netherlands

ABSTRACT

Jet engine noise is not the primary focus of investigation in static tests of aircraft engines. Because the ambient flow speed is zero, static tests are not fully representative for jet noise under flight conditions. The noise sources of interest are generated inside the engine.

Using external microphone arrays, the challenge is to categorize the internally generated noise sources based on the locations where the noise exits the engine: the intake, the bypass exhaust, and the core exhaust. However, jet noise is present at significant levels and may deteriorate the analysis.

In this paper, static tests on a small turbofan engine in an anechoic environment are considered. Acoustic measurements were conducted with linear microphone arrays parallel to the engine axis. Using CLEAN-SC a directivity breakdown was made of the engine noise sources.

Jet noise sources detected by beamforming may appear at the core exhaust and the bypass exhaust, or even upstream, thus deteriorating the CLEAN-SC results for core noise and bypass noise. A strategy to minimize the impact of jet noise is proposed, taking advantage of the short correlation length of jet noise in the far field.

NOMENCLATURE

COP	Coherent Output Power	$\mathbf{C}_v$	CSM per integration area
CB	Conventional Beamforming	$\mathbf{D}$	dirty CSM
CSM	cross-spectral matrix	f	frequency
PWL	Sound Power Level	$\mathbf{g}_j$	steering vector
B_j	source power	$\mathbf{h}$	source component
$\mathbf{C}$	CSM	i	imaginary unit
$\mathbf{C}_j$	CSM per grid point	j	grid index

k	grid index (peak location)	Δt	time delay
N	number of microphones	ν	integration area index
n	microphone index	φ	loop gain
$\vec{x}_n$	microphone location	$\vec{\xi}_j$	scan grid point

1 INTRODUCTION

Taking measurements during an aircraft flyover with a microphone array beneath the flight path is an obvious approach to quantify the relative importance of individual noise sources such as engines, flaps, slats, and landing gears [1]. However, to study the details of engine noise, static tests are more suitable. Typically, engine static tests are conducted in a test hall or on an open-air test bed, with the engine equipped with an inlet turbulence control screen and raised to sufficient height to minimize ground effects.

External acoustic measurements are often performed using a one-dimensional array of microphones on a line parallel to the engine axis. With such an array, CLEAN-SC has proven capable of decomposing the noise data into contributions from the intake, the bypass exhaust, the core exhaust, and the jet turbulence [2]. The decomposition is obtained microphone by microphone, thus yielding the directivity of each of the four sources.

Other array processing methods that can provide source directivity breakdowns are SODIX [3,4] and AFINDS [5-9]. If, in addition, pressure sensors are mounted in the intake or in one of the outlets, the corresponding directivity can be obtained with an appropriate Coherent Output Power (COP) approach [10]. Recently, a three-way comparison was made between estimates of core noise directivity obtained with AFINDS, CLEAN-SC, and COP [11]. A good agreement was found.

This paper zooms in into jet noise. In static engine tests, jet engine noise is typically not the primary object of investigation. Because the ambient flow speed is zero, static tests are not fully representative for jet noise under flight conditions. However, particularly at high engine speeds, the jet noise contribution to the total noise can be substantial, thereby complicating the assessment of the contributions of the other noise sources. Our aim is therefore to minimize the impact of jet engine noise.

In various respects, jet engine noise differs from the other noise sources:

a) The noise sources are not local, but spread over a plume behind the engine. The sources are convected downstream and have certain spatial coherence length [12]. Therefore, CLEAN-SC images will look different from the well-known images with local sources [13].
b) The spatial coherence of jet noise radiating at different angles into the far field reduces rapidly with angular spacing [14-16].
c) The directions normal to the far-field acoustic waves may not point towards the source, but more upstream. In other words, the locations found via beamforming may not agree with the actual source locations.

In this paper a strategy is proposed to minimize the influence of the impact of jet noise on the CLEAN-SC directivity of the other sources. To this end, use is made of the limited far-field coherence of jet noise. The strategy is applied to measurements of 2019 on NASA's DART turbofan engine [17].

This paper is structured as follows. Chapter 2 summarizes the use of CLEAN-SC for obtaining source directivity breakdowns. Chapter 3 describes the features of NASA's test setup. Chapter 4 highlights the challenges arising from the presence of jet noise and Chapter 5 describes how to address these. Chapter 6 presents some results and Chapter 7 summarizes the conclusions.

2 CLEAN-SC FOR DIRECTIVITY BREAKDOWN

2.1 Full CSM

The starting point of CLEAN-SC is Conventional Beamforming (CB), which is defined by the frequency-domain expression

$$B_j = \mathbf{g}_j^* \mathbf{C} \mathbf{g}_j \,. \tag{1}$$

Herein, $\mathbf{C}$ is the cross-spectral matrix (CSM), which is a Hermitian $N \times N$ matrix, with N the number of microphones. The beamforming output B_j is called "source power." The vector $\mathbf{g}_j$ is the $N \times 1$ steering vector containing the phase delays between the microphone locations $\vec{x}_n$ and the scan points $\vec{\xi}_j$:

$$g_{j,n} = \frac{1}{N} \exp\left(-2\pi i f \Delta t\left(\vec{\xi}_j, \vec{x}_n\right)\right), \tag{2}$$

where f is the frequency and $\Delta t\left(\vec{\xi}_j, \vec{x}_n\right)$ the time delay. In quiescent air, the time delay is the distance divided by the sound speed. The asterisk in Eq. (1) denotes complex conjugation.

Note that the steering vectors defined by Eq. (2) do not contain amplitude corrections for distance. Hence, the beamforming output is "as measured by the array."

The main idea of CLEAN-SC [13] is to locate sources using CB and to extract corresponding cross-spectral data from the cross-spectral matrix CSM. For that purpose, the "dirty CSM" $\mathbf{D}$ and the "CSM per grid point" $\mathbf{C}_j$ are introduced. The following iteration scheme is used:

0. Set $\mathbf{D} = \mathbf{C}$ and $\mathbf{C}_j = \mathbf{0}$ for all grid indices j.
1. Determine the CB peak source location $k = \underset{j}{\operatorname{argmax}}\left(\mathbf{g}_j^* \mathbf{D} \mathbf{g}_j\right)$ and set $B_k = \mathbf{g}_k^* \mathbf{D} \mathbf{g}_k$.
2. Set the "source component" $\mathbf{h} = \mathbf{D}\mathbf{g}_k / B_k$.
3. Update: $\mathbf{C}_k = \mathbf{C}_k + \varphi B_k \mathbf{h}\mathbf{h}^*$ and $\mathbf{D} = \mathbf{D} - \varphi B_k \mathbf{h}\mathbf{h}^*$.
4. Go back to step 1.

Step 1 assumes beamforming with the full CSM. In step 3, φ is a user-defined "loop gain" between 0 and 1.

After termination of the iteration, usually when $\|\mathbf{D}\| \ll \|\mathbf{C}\|$, the following expression remains:

$$\mathbf{C} = \mathbf{D} + \sum_{j=1}^{J} \mathbf{C}_j \,. \tag{3}$$

Thus, each grid point is associated with a CSM. Acoustic images can be constructed by considering, per grid point j, the average levels of the diagonal elements of $\mathbf{C}_j$.

The scan grid can be subdivided into "integration areas," each of which corresponds to a typical noise source. The summation in Eq. (3) can be grouped per integration area, yielding a CSM for each area:

$$\mathbf{C} = \mathbf{D} + \sum_{v} \mathbf{C}_v \,. \tag{4}$$

The diagonal elements of $\mathbf{C}_v$ contain the intended directivity information per noise source. "Source Power Integration" results [18] can be obtained by averaging the diagonals of $\mathbf{C}_v$.

2.2 Incomplete CSM

As described in [13], both CB and CLEAN-SC can be performed with an incomplete CSM, for example with the diagonal removed. Then, the CB expression becomes

$$B_j = \mathbf{g}_j^* \bar{\mathbf{C}} \mathbf{g}_j , \tag{5}$$

with $\bar{\mathbf{C}}$ the incomplete CSM and

$$g_{j,n} = \frac{1}{\bar{N}} \exp\left(-2\pi i f \Delta t\left(\vec{\xi}_j, \vec{x}_n\right)\right), \tag{6}$$

where $\bar{N}$ is the square root of the number of cross-spectra remaining in $\bar{\mathbf{C}}$.

The CLEAN-SC procedure is the same as in Section 2.1. Only the source component in step 2 is now obtained by solving

$$\mathbf{h} = \frac{1}{\sqrt{1 + \mathbf{g}_k^* \mathbf{H} \mathbf{g}_k}} \left(\frac{\bar{\mathbf{D}} \mathbf{g}_k}{B_k} + \mathbf{H} \mathbf{g}_k \right), \tag{7}$$

with

$$\mathbf{H} = \mathbf{h}\mathbf{h}^* - \overline{\mathbf{h}\mathbf{h}^*} . \tag{8}$$

Eq. (7) can solved iteratively, starting with $\mathbf{h} = \bar{\mathbf{D}} \mathbf{g}_k / B_k$.

3 NASA DART MEASUREMENTS

DART is a DGEN 380 engine (Fig. 1) used for experimental research at NASA Glenn's AAPL facility [19]. This facility features a dome which is acoustically treated to provide an anechoic environment. The DGEN 380 is a small high-bypass ratio geared turbofan engine. Its key dimensions are:

- Fan diameter: 0.36 m.
- Core duct diameter at exhaust: 0.225 m, hub-tip ratio: 0.76.
- Bypass duct diameter at exhaust: 0.45 m, hub-tip ratio: 0.78.
- Distance between core exhaust and intake: 1.22 m.
- Distance between core and bypass exhaust: 0.32 m.
- Bypass ratio: 7.6.

The measurements in 2019 were performed with three microphone arrays:

- LA088: A linear array of 61 microphones parallel to the engine axis, at 2.24 m (88") horizontal distance. The array length is 7.74 m. The microphones were placed at approximately equal polar angle steps, between 31° and 147°.
- LA148: A second linear array of 61 microphones parallel to the engine axis, at 3.76 m (148") horizontal distance. The microphone layout is different from the LA088 array layout, but the total length is almost the same: 7.78 m.
- FFOVH: A far-field overhead polar array of 24 microphones. The distance between the engine and the microphones varies from 11 m to 17 m.

A sketch with the microphone array locations can be found in Fig. 2.

Measurements were performed at various engine speeds. All signals were recorded synchronously at 100 kHz sampling frequency. The acquisition time per measurement was approximately 60 seconds.

Fig. 1 DGEN 380

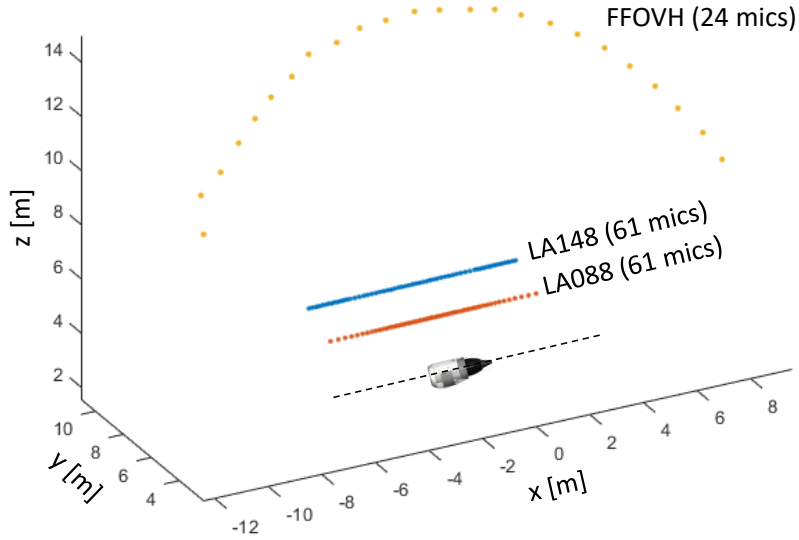

Fig. 2 DGEN 380 and microphone arrays in the AAPL

4 THE JET NOISE CHALLENGE

4.1 Typical beamforming results

Beamforming as described in Section 2 was done with the LA088 array and the engine at 80% speed. A one-dimensional scan grid on the engine axis was used, ranging from $x = -2$ m to $x = +3$ m. The core exhaust is positioned at $x = 0$, the jet flow is in positive x-direction. The grid spacing is 1 cm. CLEAN-SC was applied with $\varphi = 0.01$ loop gain. The levels are scaled to 1 m from the core exhaust (at $\vec{\xi}_0$) by adding

$$20 \times \log 10 \left(\frac{1}{N} \sum_{n=1}^{N} \left\| \vec{x}_n - \vec{\xi}_0 \right\| \right) \text{ dB}. \tag{9}$$

The CSM was obtained with Welch's method [20], including 50% overlapping snapshots and Hanning window with energy-preserving scaling. The snapshot length was 4000 samples, which implies a frequency bandwidth of 25 Hz.

Typical results of CB and CLEAN-SC, obtained with the full CSM, are shown in Fig. 3 and Fig. 4, respectively. The vertical dashed lines indicate from left to right the positions of the intake, the bypass exhaust, and the core exhaust. Noise sources are observable around each of

these locations. Tones can be seen at 2500 Hz (the main rotor blade-passing frequency), around 5000 Hz, and at some low frequencies (turbine tones). All other sources are broadband noise.

The CLEAN-SC image (Fig. 4) looks different than typical CLEAN-SC images, which show a small number of well-localized sources [13]. Downstream of the core exhaust, there is a distribution of sources due to jet noise. The jet noise sources in Fig. 4 are organized in striations that appear to extend upstream through the core exhaust and the bypass exhaust. In other words: bypass noise and core noise are mixed with jet noise, which poses a challenge for source separation.

The jet noise striations are located even before the bypass exhaust, which seems to contradict physics. In other words, there is discrepancy between the actual source locations and the locations found by beamforming.

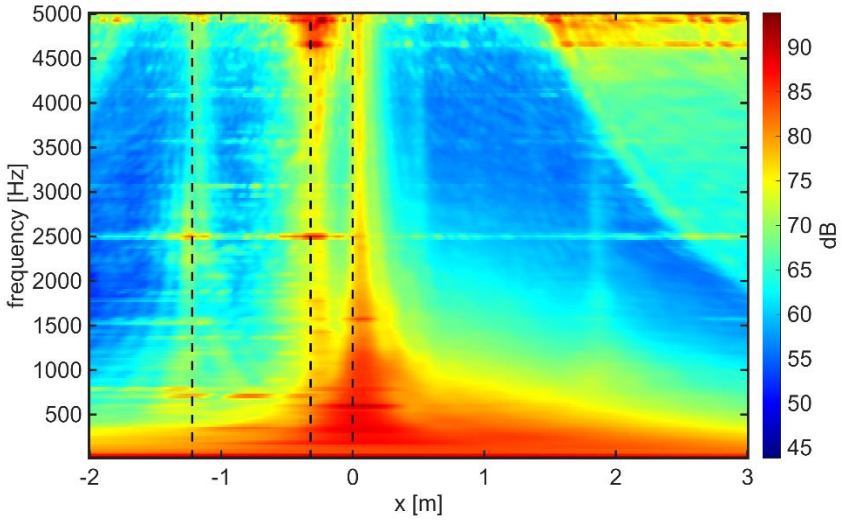

Fig. 3 CB image, LA088 array, 80% speed, full CSM

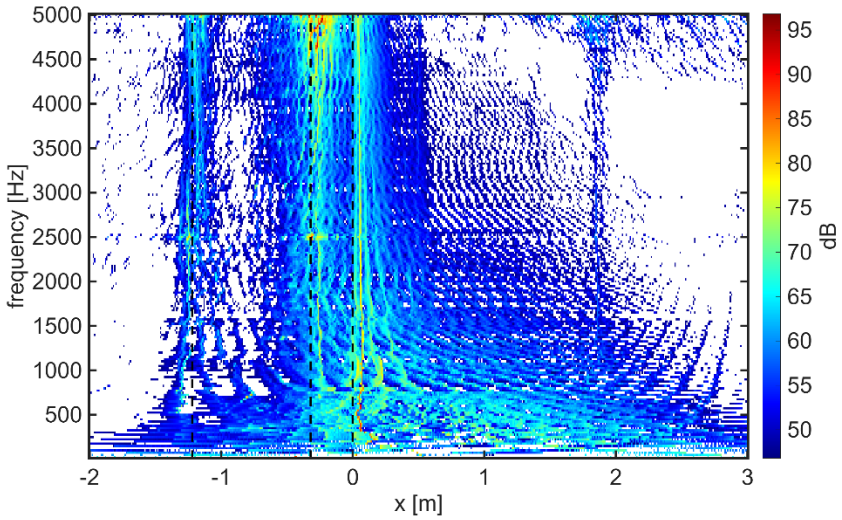

Fig. 4 CLEAN-SC image, LA088 array, 80% speed, full CSM

4.2 Jet noise source location mismatch

The mismatch between beamformed and actual source locations is confirmed by simulations in which the jet is modelled by acoustic sources on the engine axis, having prescribed spatial coherence. Mathematical details of the wave packet model can be found in Appendix A.

The acoustic field radiated from a typical wave packet, centered around $x = 0$, is depicted in Fig. 5. The wave packet is given by Eq. (37) in Appendix A. The coherence length is $L = 0.4$ m, the frequency $f = 600$ Hz, and the convection speed $U = 130$ m/s. The sound speed c was set to 340 m/s. The image was obtained by numerically evaluating the integral in Eq. (38). In Fig. 5, short hydrodynamic waves can be recognized around the wave packet. Further away from the source, the wave lengths have become acoustic.

Fig. 5 also shows the microphone positions of the LA088 array. Using the simulated array data, CB was performed with the scan grid on the source line ($y = 0$). The results are shown in Fig. 6, together with the actual source strengths of Eq. (37). The beamformed source peak is located at $x = -0.43$ m, which is clearly upstream of the actual source peak, like part of the sources in Fig. 4.

The mismatch in the source location is a near-field effect: when the array is moved further away from the source line, the mismatch vanishes. This has been confirmed by simulations, but follows as well from the analysis in Appendix A.4. It is also visible, albeit not very clearly, in the CLEAN-SC image of Fig. 7, obtained with the more distantly placed LA148 array. In Fig. 7, the levels of the sources between the bypass exhaust and the core exhaust are lower than in Fig. 4. Moreover, the entire pattern of the jet noise sources appears to be shifted to the right.

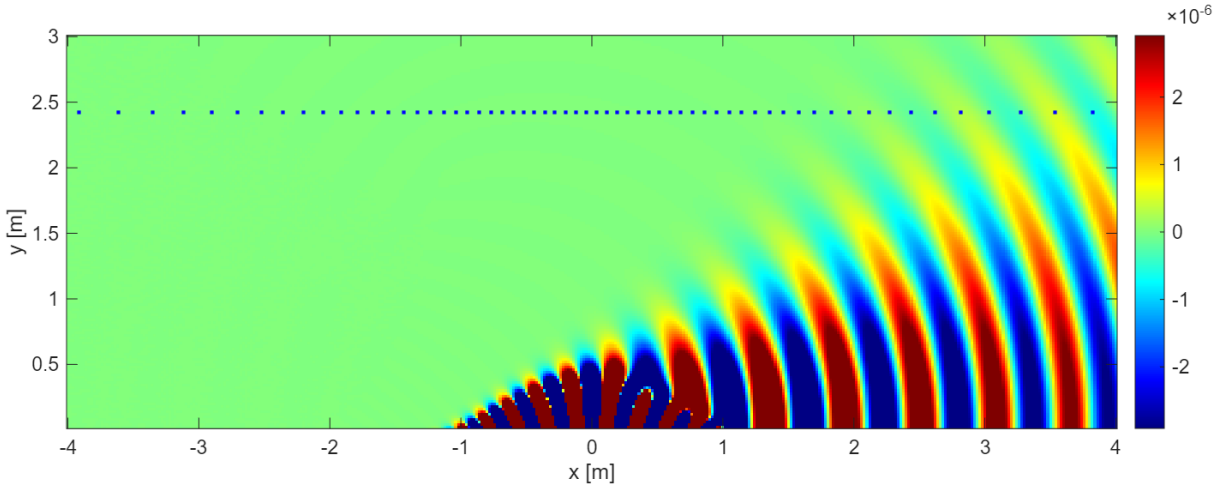

Fig. 5 Simulation of acoustic field radiating from wave packet

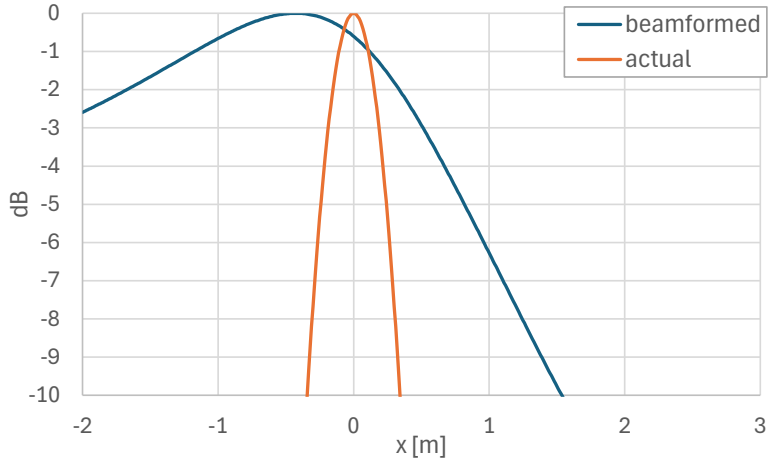

Fig. 6 CB output with simulated wave packet data

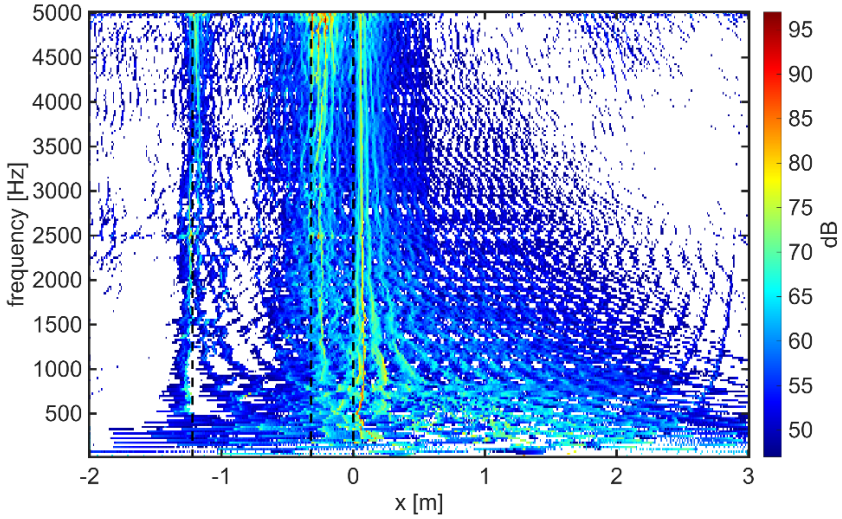

Fig. 7 CLEAN-SC image, LA148 array, 80% speed, full CSM

5 CLASSIFICATION OF NOISE SOURCES

To decompose the total noise into the different engine noise components, CLEAN-SC must link, per frequency, each grid point to one of the sources. In other words, the scan grid must be subdivided into integration areas per noise source. However, jet noise may be detected in each integration area. To minimize the impact of this, the integration areas of intake, bypass exhaust, and core exhaust should be as small as possible, i.e., not larger than necessary.

To make the source locations clearer, we can use CSM diagonal removal. The CLEAN-SC image corresponding to Fig. 4 is shown in Fig. 8. There is a clear reduction in jet noise, while the levels of the other sources appear to remain the same.

The reason for this reduction of jet noise is the short correlation length in the far field [14-16]. To further utilize this property, the secondary diagonal of the CSM (directly above and below the main diagonal) is also removed also. Thereby, the cross-spectra between neighboring microphones are excluded, which should further reduce noise with short correlation length.

The CLEAN-SC image after removal of the secondary CSM diagonal is shown in Fig. 9. As expected, the jet noise has decreased further. In fact, significantly further. This also applies to

the sources upstream of the bypass exhaust, providing additional evidence that these are due to jet noise.

Note that the intake levels in Fig. 9 are also lower than in Fig. 8. Hence, although removing multiple CSM diagonals is highly effective in isolating local noise sources from jet noise, this approach can be too aggressive to retrieve the correct levels. Furthermore, Fig. 9 shows spurious sources in the upper right part of the image.

The difference between Fig. 4 and Fig. 9 is shown in Fig. 10. This image therefore only shows the (jet noise) sources with short far-field correlation length.

The results obtained with three and four CSM diagonals removed are shown in and Fig. 11 and Fig. 12, respectively. In Fig. 12 the jet noise sources have disappeared completely, except at the lowest frequencies (below 500 Hz).

The images in the previous section led to the classification shown in Fig. 13, in which the integration areas were kept as small as possible. Further, frequency-dependent refinement is still possible. The purple area is intended to capture a few turbine tones that appear to radiate from the nacelle.

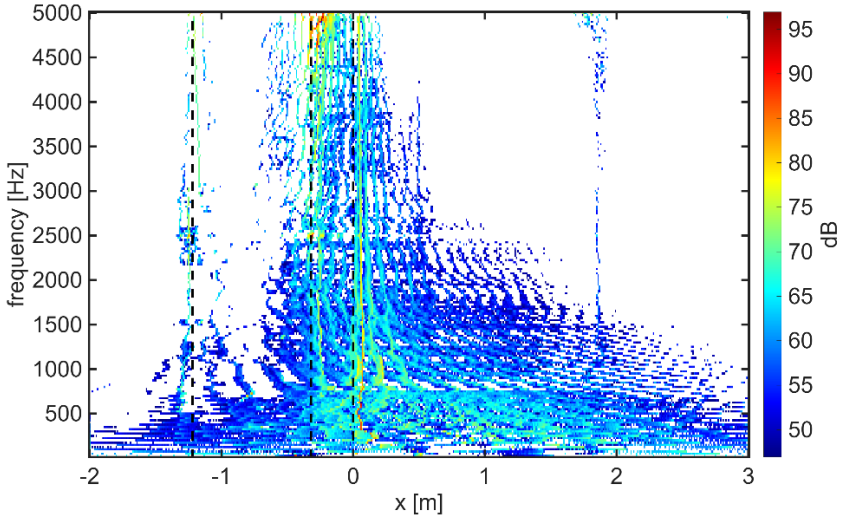

Fig. 8 CLEAN-SC image, LA088 array, 80% speed, CSM diagonal removed

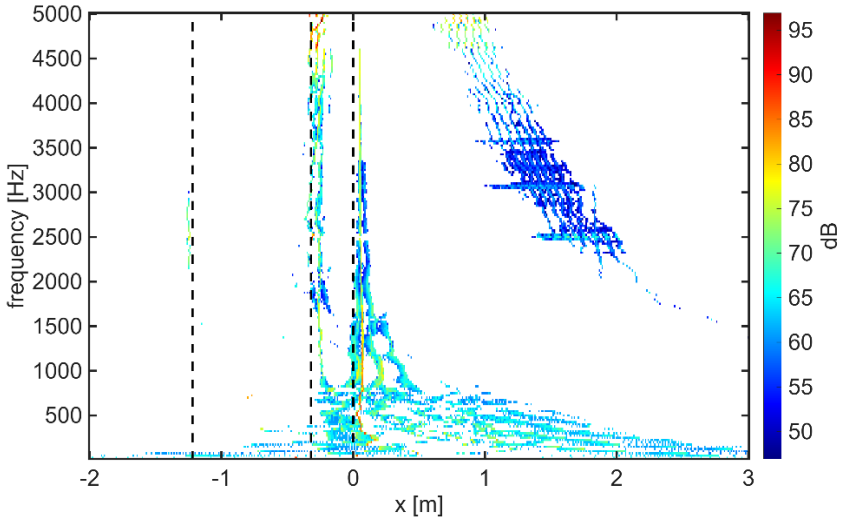

Fig. 9 CLEAN-SC image, LA088 array, 80% speed, two CSM diagonals (upper and lower) removed

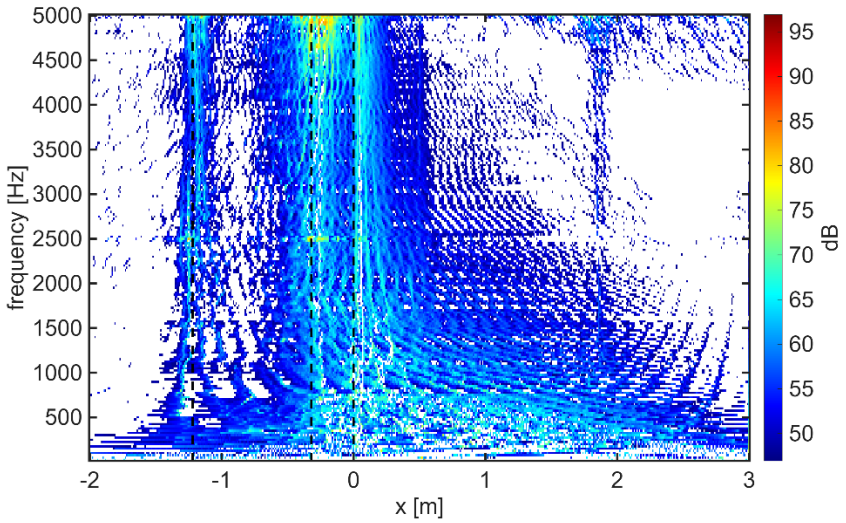

Fig. 10 Difference between Fig. 4 and Fig. 9

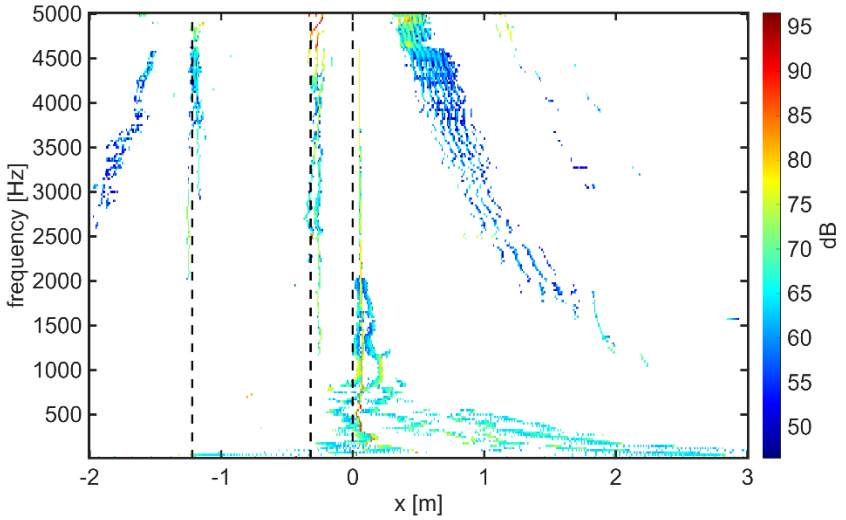

Fig. 11 CLEAN-SC image, LA088 array, 80% speed, three CSM diagonals (upper and lower) removed

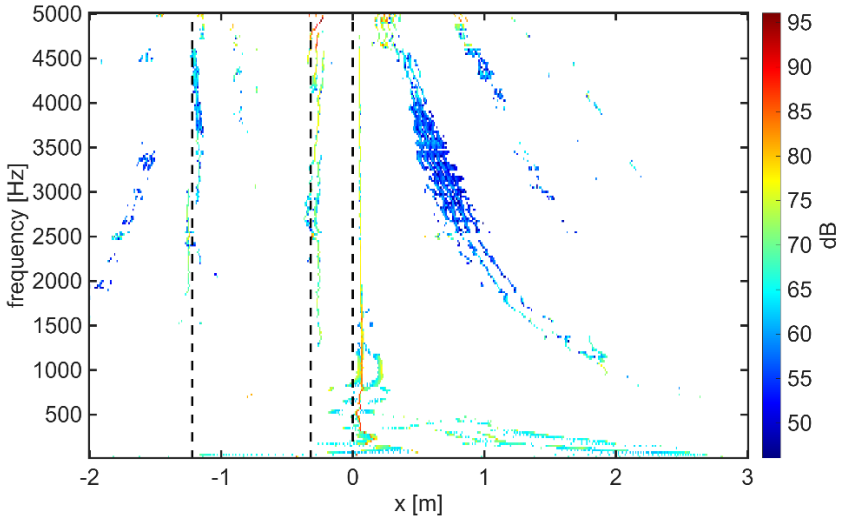

Fig. 12 CLEAN-SC image, LA088 array, 80% speed, four CSM diagonals (upper and lower) removed

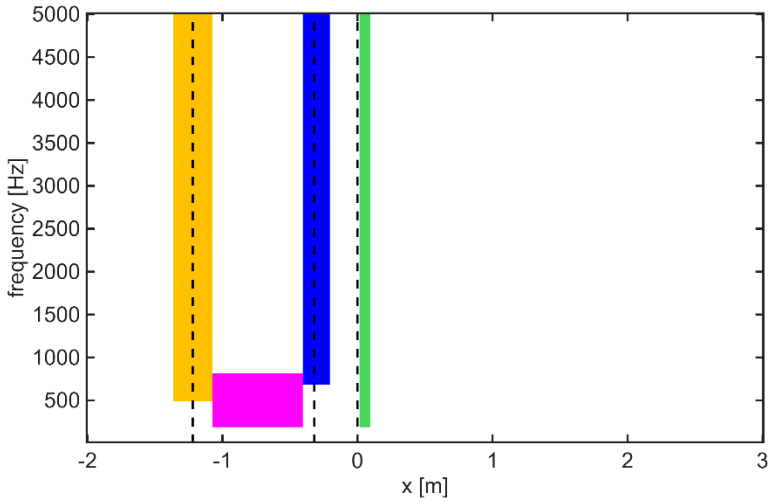

Fig. 13 CLEAN-SC classification, LA088 array, 80% speed (orange = intake, blue = bypass, green = core, purple = nacelle, white = jet)

6 RESULTS

A typical full-CSM CLEAN-SC directivity breakdown at 3150 Hz (1/3 octave band) is shown in Fig. 14. The polar angles at the *x*-axis are relative to the core exhaust. For each microphone, the levels have been corrected to 1 m from the core exhaust. The summation of the four contributions is almost perfectly aligned with the measured SPL. More results, including comparisons with other methods and other arrays, can be found in [11].

Fig. 15 shows the effects of removing one and two diagonals. The symbols represent the full-CSM results; the straight lines correspond to standard diagonal removal; the dashed lines were obtained after the additional removal of the secondary diagonal. The figure shows that removing the main diagonal only affects the jet noise levels. The effects of removing the secondary diagonal are greater.

By comparing the full-CSM results with standard diagonal removal, we can conclude that jet noise has a negligible influence on the directivities of the other noise sources, because the effects of jet noise reduction are not noticeable. Apparently, the integration areas are sufficiently small at this frequency.

For the entire frequency range we consider the Sound Power Level (PWL), which is the average microphone level after scaling to 0.282 m from the core exhaust. The results are shown in Fig. 16. There is hardly any difference between the PWL without and with (main) diagonal removal, except for jet noise for which the deviation begins around 2000 Hz. For core noise, the removal of the second CSM diagonal does not lead to reduction below 2500 Hz.

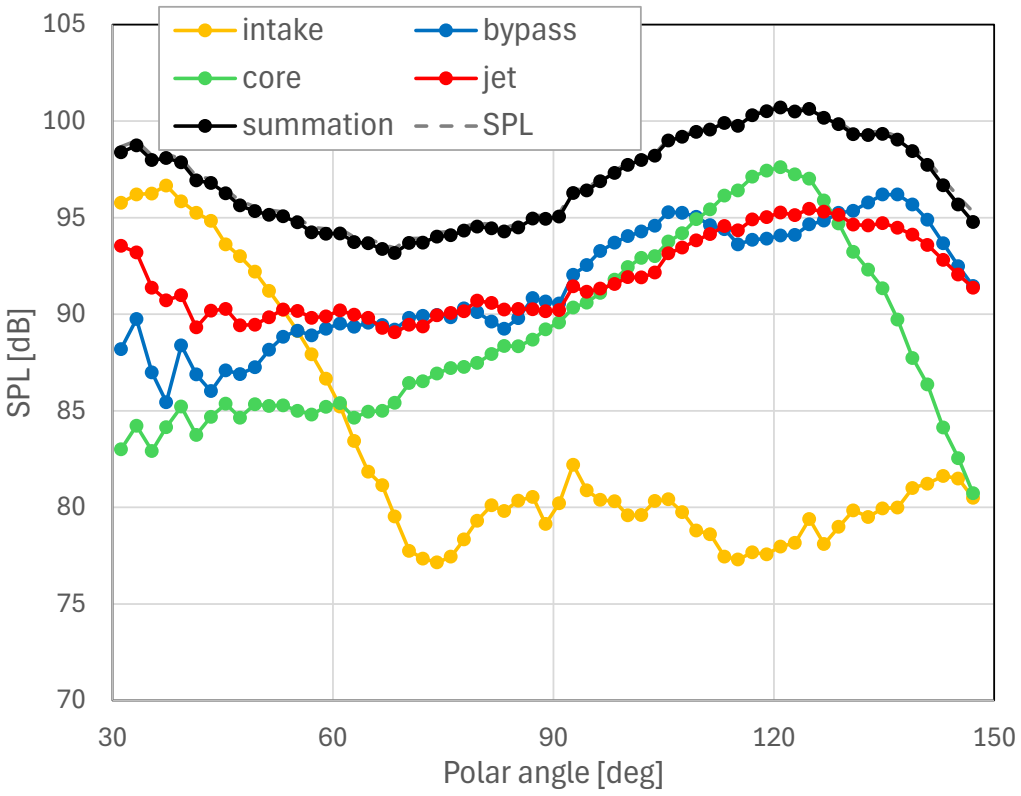

Fig. 14 Directivity breakdown, LA088 array, 80% speed, 3150 Hz (1/3 octave), full CSM

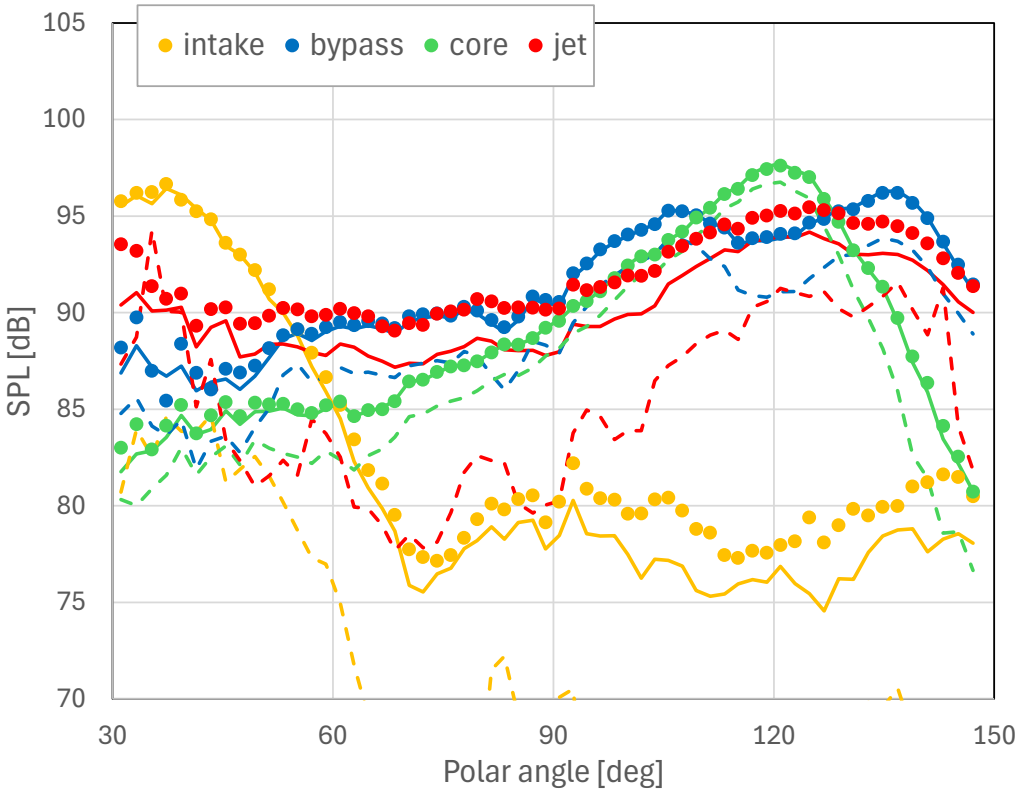

Fig. 15 Directivity breakdown, LA088 array, 80% speed, 3150 Hz (1/3 octave); symbols: full CSM, solid lines: main diagonal removed, dashed lines: main and secondary diagonals removed

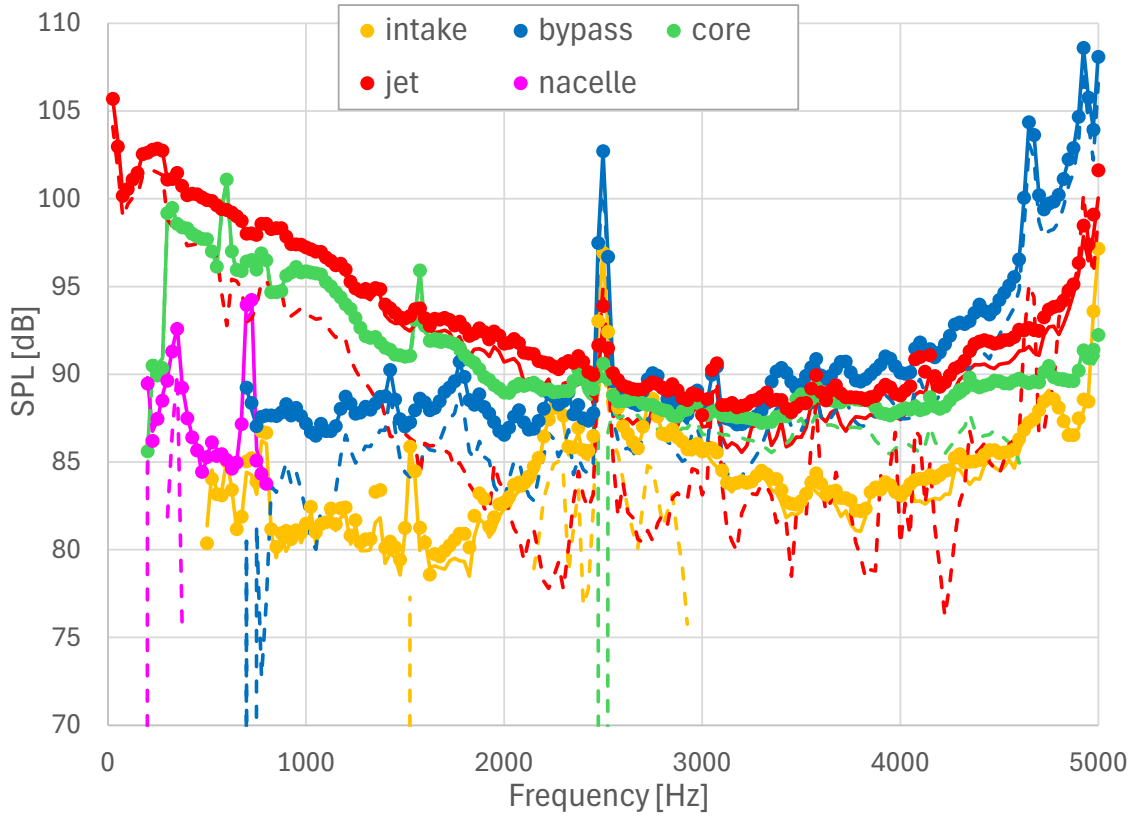

Fig. 16 PWL breakdown, LA088 array, 80% speed; symbols: full CSM, solid lines: main diagonal removed, dashed lines: main and secondary diagonals removed

7 CONCLUSIONS

With a sideline microphone array at a static engine test, CLEAN-SC can estimate the level and the directivity of the different noise components: intake, bypass, core, and jet noise. Jet noise differs significantly from the other sources and may hamper the determination of their directivities. CLEAN-SC may detect jet noise at the same locations as bypass and core noise. Jet noise may appear even more upstream.

To minimize the impact of jet noise, the integration areas of the other sources must be as small as possible. Multiple CSM diagonal removal proved to be an effective approach for removing jet noise from the images, thus utilizing the short correlation length of jet noise in the far field. By applying CLEAN-SC with multiple diagonal removal, precise locations of the other sources become clear, thus enabling the definition of small integration areas.

Application to NASA static engine measurements showed that this approach is successful.

ACKNOWLEDGEMENTS

This research was funded by the AeroAcoustics Research Consortium (AARC) under contract number OAI-AARCP-24127. Lennart Hultgren of NASA GRC is gratefully acknowledged for providing the measured data.

REFERENCES

[1] Sijtsma, P., and Wal, H.M.M. van der, "Identification of Noise Sources on Civil Aircraft in Approach Using a Phased Array of Microphones," NATO Paper SET-079-24, published in RTO-MP-SET-079, 2004.

[2] Sijtsma, P., "Using CLEAN-SC for Determining the Directivity of Engine Noise Sources," AIAA Paper 2023-3839.

[3] Michel, U., and Funke, S., "Noise Source Analysis of an Aeroengine with a New Inverse Method SODIX," AIAA Paper 2008-2860.

[4] Oertwig, S., Siller, H.A., Schumacher, T., and Funke S., "Extension of the Source Localization Method SODIX for the Determination of Partially Coherent Sound Sources," AIAA Paper 2022-2812.

[5] Tester, B.J., Ricoup, T., and Gabard, G., "Extracting Engine Noise Source Levels from Phased Arrays with Improved Internal Source Models and Evaluation Against Simulated and Measured Data," AIAA Paper 2012-2272.

[6] Tester, B.J., "Engine Noise Source Breakdowns from an Improved Inverse Method (AFINDS) of Processing Phased Array Measurements," AIAA Paper 2014-3067.

[7] Tester, B.J., "An Improved Inverse-Phased Array Method for Estimating Free-Field Engine Core Noise Spectra from Measurements in Reverberant Test Cells," ICSV24, London, 2017.

[8] Tester, B.J., Ekoule, C.M., and Quaranta, E., "An Improved Phased Array Method for Estimating Free-Field Engine Core Noise Spectra from Test Cell Measurements on Short Cowl Engines," AIAA Paper 2019-2699.

[9] Tester, B.J., Funke, S., Britchford, K.M., and Knighton, C.J., "Application of a Noise Source Separation Method (AFINDS) to External Array Measurements Taken on Short Cowl Engines in Anechoic, Outdoor, and Indoor Facilities," AIAA Paper 2022-2811.

[10] Sijtsma, P., Dreux, M., Delescluse, B., Leneveu, R., and Mardjono, J., "Coherent Output Power with Groups of Microphones," AIAA Paper 2024-3330.

[11] Sijtsma, P., and Tester, B.J., "Cross-Comparison of Engine Noise Directivity Estimates with AFINDS, CLEAN-SC and COP," AIAA Paper 2026-3558.

[12] Michalke, A., "On the Effect of Spatial Source Coherence on the Radiation of Jet Noise," *Journal of Sound and Vibration*, Vol. 55, No. 3, 1977, pp. 377-394.

[13] Sijtsma, P., "CLEAN Based on Spatial Source Coherence," *International Journal of Aeroacoustics*, Vol. 6, No. 4, 2007, pp. 357-374.

[14] Ahuja, K.K., "Designing Clean Jet Noise Research Facilities and Making Accurate Jet Noise Measurements," *International Journal of Aeroacoustics*, Vol. 2, Nos. 3 & 4, 2003, pp. 371-412.

[15] Cavalieri, A.V., and Agarwal, A., "Coherence Decay and its Impact on Sound Radiation by Wavepackets," *Journal of Fluid Mechanics*, Vol. 748, 2014, pp. 399–415.

[16] Sirotto, J.R., Cordioli, J.A., and Cavalieri, A.V., "Analysis of Far-Field Coherence of Subsonic Jet Noise," AIAA Paper 2018-2977.

[17] Hultgren, L.S., Boyle, D.K., and Henderson, B.S., "DGEN Aeropropulsion Research Turbofan Source-Diagnostic Test: Experimental Setup and Acoustic-Data Structure," NASA/TM-20205008042, 2020.

[18] Merino-Martínez, R., Sijtsma, P., Rubio Carpio, A., Zamponi, R., Luesutthiviboon, S., Malgoezar, A.M.N., Snellen, M., Schram, C., and Simons, D.G., "Integration Methods for Distributed Sound Sources," *International Journal of Aeroacoustics*, Vol. 18 (4-5), 2019, pp. 444-469.

[19] https://www.nasa.gov/centers-and-facilities/glenn/aero-acoustic-propulsion-laboratory/

[20] Welch, P. D., "The Use of Fast Fourier Transform for the Estimation of Power Spectra: A Method based on Time Averaging over Short, Modified Periodograms," *IEEE Transactions on Audio and Electroacoustics*, Vol. AU-15, No. 2, 1967, pp. 70–73.

APPENDIX A: A SIMPLE WAVE PACKET MODEL

$a(\Delta x)$	cross-power	Q	acoustic response to wave packet
c	sound speed	$s(x)$	source strength
$E\{\ldots\}$	expectation value	$w(x)$	wave packet
f	frequency	$X(x_1,x_2)$	cross-power
G	Green's function	α	Fourier variable
i	imaginary unit	δ	Dirac delta function
k	acoustic wave number	$\gamma(\Delta x)$	coherence function
k_h	hydrodynamic wave number	λ	see Eq. (43)
L	coherence length	θ	polar angle
p	acoustic pressure	$\rho(x)$	uncorrelated complex numbers
R	source-receiver distance	Ψ	see Eq. (41)
t	time		

A.1 Line source

Consider an infinite line of random noise sources located on the x-axis. At fixed frequency f, the source amplitudes are complex numbers $s(x)$. The source cross-power is

$$X(x_1,x_2)=E\left\{s(x_1)s(x_2)^*\right\}, \tag{10}$$

in which E is the expectation value and the asterisk denotes complex conjugation. It is assumed that the source line has uniform statistical properties, which implies that the cross-powers only depend on the distance between x_1 and x_2:

$$X(x_1,x_2)=a(x_1-x_2). \tag{11}$$

Thus, $a(0)$ is the auto-power.

To mimic jet noise, the cross-power is prescribed by

$$a(\Delta x)=\gamma(\Delta x)\exp(-ik_h\Delta x), \tag{12}$$

$$k_h=2\pi f/U, \tag{13}$$

with U the convection speed and γ a coherence function with the following properties:

$$\begin{cases}\gamma(0)=1,\\ \gamma(-x)=\gamma(x),\\ 0\le\gamma(x)\le 1.\end{cases} \tag{14}$$

The acoustic field $p(x,y,z)$ can be obtained from the Helmholtz equation:

$$\nabla^2 p+k^2 p=s(x)\delta(y)\delta(z), \tag{15}$$

$$k=2\pi f/c. \tag{16}$$

The solution is

$$p(x,y,z)=\iiint G(x,y,z,\xi,\eta,\zeta)s(\xi)\delta(\eta)\delta(\zeta)d\xi d\eta d\zeta, \tag{17}$$

with G the Green's function:

$$G=\frac{-1}{4\pi R}\exp(-ikR), \tag{18}$$

$$R=\left(\left(x-\xi\right)^2+\left(y-\eta\right)^2+\left(z-\zeta\right)^2\right)^{1/2}. \tag{19}$$

Eq. (17) is elaborated as

$$p\left(x,r\right)=\int G\left(x-\xi,r\right)s\left(\xi\right)d\xi\,, \tag{20}$$

with

$$\begin{cases} G\left(x,r\right)=\dfrac{-1}{4\pi R\left(x,r\right)}\exp\left(-ikR\left(x,r\right)\right), \\ R\left(x,r\right)=\sqrt{x^2+r^2},\ r^2=y^2+z^2. \end{cases} \tag{21}$$

For the cross-power between two points $\left(x_1,r_1\right)$ and $\left(x_2,r_2\right)$ we have

$$E\left\{p\left(x_1,r_1\right)p\left(x_2,r_2\right)^*\right\}=\int\int G\left(x_1-\xi_1,r_1\right)G\left(x_2-\xi_2,r_2\right)^*a\left(\xi_1-\xi_2\right)d\xi_1d\xi_2\,. \tag{22}$$

A.2 Wave packets

We are looking for a wave packet $w\left(x\right)$ such that the source distribution can be written as a random convolution:

$$s\left(x\right)=\int\rho\left(\xi\right)w\left(x-\xi\right)d\xi\,, \tag{23}$$

with $\rho\left(\xi\right)$ random complex-valued numbers without spatial correlation. Formally:

$$E\left\{\rho\left(\xi_1\right)\rho\left(\xi_2\right)^*\right\}=\delta\left(\xi_1-\xi_2\right). \tag{24}$$

Then, for the acoustic cross-power we have

$$E\left\{p\left(x_1,r_1\right)p\left(x_2,r_2\right)^*\right\}=\int Q\left(x_1,r_1,\tilde{\xi}\right)Q\left(x_2,r_2,\tilde{\xi}\right)^*d\tilde{\xi}\,, \tag{25}$$

$$Q\left(x,r,\tilde{\xi}\right)=\int G\left(x-\xi,r\right)w\left(\xi-\tilde{\xi}\right)d\xi\,. \tag{26}$$

The expression $Q\left(x,r,\tilde{\xi}\right)$ is the acoustic response to a shifted wave packet around $x=\tilde{\xi}$.

The wave packet is related to the prescribed cross-power, Eq. (12). From Eqs. (23) and (24) follows

$$X\left(x_1,x_2\right)=\int w\left(x_1-\xi\right)w\left(x_2-\xi\right)^*d\xi\,. \tag{27}$$

Thus, with Eq. (11), we have to solve

$$\int w\left(x+\xi\right)w\left(\xi\right)^*d\xi=a\left(x\right), \tag{28}$$

Spatial Fourier transformation yields

$$\left|\int\exp\left(-2\pi i\alpha x\right)w\left(x\right)dx\right|^2=\int\exp\left(-2\pi i\alpha x\right)a\left(x\right)dx\,. \tag{29}$$

Briefly,

$$\left|\hat{w}\left(\alpha\right)\right|^2=\hat{a}\left(\alpha\right). \tag{30}$$

Consequently, the Fourier transform of $a\left(x\right)$ must be real-valued and positive. A solution for $w\left(x\right)$ is found with the inverse Fourier transform:

$$w\left(x\right)=\int\exp\left(2\pi i\alpha x\right)\sqrt{\hat{a}\left(\alpha\right)}d\alpha\,. \tag{31}$$

For the right-hand side of Eq. (30) we can write, with Eq. (12):

$$\hat{a}\left(\alpha\right)=\hat{\gamma}\left(\alpha+k_h/2\pi\right), \tag{32}$$

with $\hat{\gamma}$ the Fourier transform of the coherence function.

A.3 Gaussian coherence function

Let the coherence function be gaussian [12]:

$$\gamma(x) = \exp\left(-\pi\left(\frac{x}{2L}\right)^2\right), \tag{33}$$

where L is the coherence length:

$$L = \int_0^\infty \gamma(x)\,dx\,. \tag{34}$$

The inverse Fourier transform of Eq. (33) is also gaussian:

$$\hat{\gamma}(\alpha) = 2L\exp\left(-4\pi(\alpha L)^2\right). \tag{35}$$

With Eq. (32) we have

$$\hat{a}(\alpha) = 2L\exp\left(-4\pi L^2(\alpha + k_h/2\pi)^2\right). \tag{36}$$

From Eq. (31) it follows that

$$w(x) = \frac{1}{\sqrt{L}}\exp\left(-\frac{\pi}{2}\left(\frac{x}{L}\right)^2\right)\exp(-ik_h x)\,. \tag{37}$$

Thus, the acoustic response, Eq.(26), of the non-shifted wave packet is

$$Q(x,r,0) = \frac{-1}{4\pi\sqrt{L}}\int \frac{1}{R(x-\xi,r)}\exp\left\{-\frac{\pi}{2}\left(\frac{\xi}{L}\right)^2 - i\left(kR(x-\xi,r) + k_h\xi\right)\right\}d\xi\,. \tag{38}$$

A.4 Far-field approximation

In the far field, the following approximation can be made:

$$R(x-\xi,r) = R(x,r) - \frac{x\xi}{R(x,r)} + \frac{\xi^2}{2R(x,r)}\left(1 - \frac{x^2}{R(x,r)^2}\right). \tag{39}$$

If we insert this in the exponent part of Eq. (38), and replace $1/R(x-\xi,r)$ by $1/R(x,r)$, we find

$$Q(x,r,0) = \frac{-1}{4\pi R}\frac{\sqrt{2L}}{\sqrt{1+ikL\lambda\sin^2(\theta)}}\exp\left(-\frac{\Psi}{2\pi}\right)\exp\left[-ikR\left(1 - \frac{\lambda^2\sin^2(\theta)\Psi}{2}\right)\right], \tag{40}$$

with

$$\Psi = \frac{\left(kL\cos(\theta) + k_h L\right)^2}{1 + \left(kL\lambda\sin^2(\theta)\right)^2}\,, \tag{41}$$

$$\cos(\theta) = -x/R\,, \tag{42}$$

$$\lambda = L/\pi R\,. \tag{43}$$

The term enclosed by the square brackets in Eq. (40) describes the wave fronts, i.e., the surfaces with equal phase:

$$t = \frac{R}{c}\left(1 - \frac{\lambda^2\sin^2(\theta)\Psi}{2}\right). \tag{44}$$

This is different from atmospheric expansion from a point source. The vectors normal to the wave fronts do not point to the origin. Atmospheric expansion is retrieved for $\lambda \to 0$.